

1 **Mature diffuse tectonic block boundary revealed by the 2020 southwestern**
2 **Puerto Rico seismic sequence**

3
4 U.S. ten Brink^{1*}, L. Vanacore², E.J. Fielding³, J.D. Chaytor¹, A.M. López-Venegas², W.
5 Baldwin¹, D. Foster¹, B.D. Andrews¹

6
7 1 – U.S. Geological Survey, Woods Hole Science Center, Woods Hole, MA

8 2 – Dept. of Geology, U. of Puerto Rico, Mayaguez, PR

9 3 – Jet Propulsion Laboratory, California Institute of Technology, Pasadena, CA

10 * Corresponding author: Uri ten Brink utenbrink@usgs.gov

11
12 **Key points**

13 -Seismic activity did not follow main shock-aftershock sequence and likely ruptured multiple
14 faults in SWPR

15 -Geologic indicators suggest long-term diffuse deformation due perhaps to heterogenous arc
16 composition

17 -This zone may be the southernmost domain of a diffuse deformation boundary between
18 Hispaniola and Puerto Rico

19
20 **Abstract**

21 Distributed faulting typically tends to coalesce into one or a few faults with repeated
22 deformation. The 2020 seismic sequence in southwestern Puerto Rico (SWPR) was characterized
23 however by rupture of several short intersecting strike-slip and normal faults, although several
24 lines of geological and morphological evidence suggest repeated deformation since post early

25 Pliocene (\sim >3 Ma). We mapped these faults by acquiring high-resolution seismic reflection
26 profiles, by modeling shoreline subsidence and displacement from InSAR, and by tracking the
27 progression of clustered medium-sized (\geq Mw4.5) earthquakes. The faults underlie the insular
28 shelf and upper slope in the vicinity of Guayanilla submarine canyon. This deformation may
29 represent the southernmost part of a diffuse boundary, the Western Puerto Rico Deformation
30 Boundary, which accommodates differential movement between the Puerto Rico and Hispaniola
31 arc blocks. This differential movement is probably driven by the differential seismic coupling
32 along the Puerto Rico – Hispaniola subduction zone. We propose that the compositional
33 heterogeneity across the island arc retards the process of focusing the deformation into a single
34 fault. Given the evidence present here, we should not expect a single large event in this area but
35 similar diffuse sequences in the future.

36

37 **1. Introduction**

38 The seismic activity in southwestern Puerto Rico (SWPR) (Fig. 1) consisted of +13,000
39 earthquakes ($M \geq 2.5$) with 43 earthquakes with $M_w \geq 4.5$ since its start on December 28, 2019.
40 The largest of these events, an Mw6.4 on Jan. 2020 was located offshore and had a mixed normal
41 and strike-slip motion (Liu et al., 2020, ANSS-ComCat). The earthquake sequence and in
42 particular the Mw6.4 earthquake caused extensive damage in coastal towns (Morales-Velez et
43 al., 2020; Miranda et al., 2020; Von Hillebrandt et al., 2020), co-seismic subsidence around
44 Guayanilla Bay (Allstadt et al., 2020; Fielding et al., 2020; Pérez-Valentín et al., 2021),
45 liquefaction, ground failures, and the collapse of an iconic coastal rock bridge (López-Venegas et
46 al., 2020a, 2020b, Allstad et al., 2020; Pérez-Valentín et al., 2021). The prolonged seismic
47 activity had thus created anxiety among the island's population. The activity was centered

48 around a defunct oil refinery and strategic facilities for the island, such as a liquid natural gas
49 terminal, an electric power station.

50

51 The seismic activity as expressed in the earthquakes' b-value is not a typical foreshock, main
52 shock, and aftershock sequence ([Dascher-Cousieau et al., 2020](#)). Based on the time series of the
53 b-values, Dascher-Cousieau et al. (2020) interpreted the earthquake activity to indicate that the
54 observed seismic activity to date is part of a foreshock sequence with a larger main shock yet to
55 come. An alternative view which we discuss here is that the seismic activity represents the
56 rupture of small faults, that are part of a diffuse block boundary within the Greater Antilles
57 island arc. A similar diffuse block boundary with associated sequences of seismic activity had
58 been suggested for the 70-100-km-wide Central Costa Rica Deformed Belt across the Costa Rica
59 volcanic arc, which separates the middle America subduction zone from the Panama Block
60 ([Marshall et al., 2000](#)).

61

62 Deformation due to the seismic activity in SWPR appears to have occurred throughout the
63 Pleistocene (and perhaps part of the Pliocene) and is not a recent phenomenon (e.g., [Mann et al.,
64 2005; Prentice, 2005; Piety et al., 2018](#)). The evidence discussed here raises the question of
65 whether there are some tectonic boundaries where deformation remains diffuse over long periods
66 of geologic time and does not coalesce into one or few mature faults and if so, why. This
67 question is important to understanding and predicting seismic hazard.

68

69 We address here the following questions: 1. Can we identify the faults responsible for the
70 seismic sequence?.2 Is the activity organized in a predictable way? 3. Is it a recurring activity?

71 4. What framework tectonics generated this activity?

72

73 Most of the seismic activity during this seismic sequence occurred offshore, which complicated
74 the search for the ruptured faults. Mapping faults therefore relied on several lines of evidence: (a)
75 Mapping faults in the shallow sub-seafloor by marine high-resolution seismic reflection survey
76 and evaluating seafloor geomorphology; (b) Matching vertical and horizontal displacement
77 models to observed InSAR coastal deformation around the January 7, 2020 Mw6.4 earthquake
78 and the July 3, 2020 Mw5.3 earthquake; (c) Identifying clusters of medium earthquakes and
79 drawing possible faults based on their focal mechanisms.

80

81 **2. Background**

82 Puerto Rico and Hispaniola are part of the inactive Mesozoic and early Cenozoic Greater
83 Antilles island arc that accommodated southwestward subduction of the North American plate
84 under the Caribbean plate. Subduction direction changed to WSW starting ~40 Myr ago resulting
85 in a very oblique convergence along the trench north of Puerto Rico (Fig. 1; DeMets et al.,
86 2000). Muertos Trough, a wedge of deformed sediment south of the island accommodates
87 thrusting of the arc over the interior Caribbean plate, likely in a sub-perpendicular orientation
88 (ten Brink et al., 2009).

89

90 The 2020 seismic sequence occurred mostly under the insular shelf and slope south of Puerto
91 Rico (Fig. 1). The slope there is dissected by the tributaries of Guayanilla Canyon, which cuts
92 down through unconsolidated Quaternary deposits, the middle Miocene to Early Pliocene shelf
93 carbonates of the Ponce Formation and the deeper Juan Diaz Formation chalks (Trumbull and

94 [Garrison, 1973](#)). The Guayanilla canyon system is the only significant submarine drainage along
95 the south coast of Puerto Rico. The canyon system has eroded into the insular shelf, forming an
96 asymmetric amphitheater ([Fig. 1, 2](#)). West and east of this canyon system, the shelf edge is
97 oriented roughly W-E and canyon systems are undeveloped. The shelf width is ≤ 12 km west and
98 ≤ 18 km east of the canyon area, respectively, but is as narrow as 1 km in the canyon area, where
99 shallow channels dissect the reef structures.

100

101 Very few faults have been mapped on shore in the vicinity of the recent seismic activity. Mid-
102 Holocene faults were trenched in Lajas Valley ([Prentice et al. 2005](#)) and near Ponce ([Piety et al.](#)
103 [2018](#)). A fault, named San Francisco Fault, which can be extrapolated into Guayanilla Bay was
104 suggested by [Grossman \(1963\)](#) from surface geology. A 33-km-long left-lateral strike-slip fault
105 stretching from Punta Montalva to north Boquerón Bay on the west coast of Puerto Rico was
106 postulated mostly based on morphology by [Roig-Silva et al. \(2013\)](#) ([Fig. 3](#)). [Garrison \(1969\)](#)
107 interpreted a several-hundred-milliseconds-deep half graben in Sparker seismic reflection data on
108 the insular shelf south of Ponce. The graben is bounded by the Caja de Muertos Fault on the SE
109 and possibly the Bajo Tasmanian Fault on the NW ([Fig. 2](#)). Caja De Muertos Island was
110 proposed to have been uplifted by faulting ([Kay, 1957](#)) A narrow elongate bathymetric trough at
111 the upper slope south of the island, named Investigator Fault, was previously considered a left-
112 lateral strike-slip fault, but high-resolution multibeam bathymetry, seismic reflection data
113 ([Granja-Bruña et al., 2009](#); [ten Brink et al., 2009](#)) and an ROV dive in 2015 ([Kennedy et al.,](#)
114 [2015](#)) suggest that this trough is either inactive or that it is formed by a N-S extension. The area
115 of seismic activity is largely devoid of good quality seismic reflection data.

116

117 3. Data

118 We conducted a high-resolution multichannel seismic survey between March 7-13, 2020 aboard
119 the University of Puerto Rico's R/V Sultana based at the Marine Sciences laboratory at
120 Magueyes Island (Fig. 2 and 4) in La Parguera. The seismic sources included a 2.4 kJ Sparker at
121 water depths >500 m, a 1 kJ Sparker at water depths of 100-500 m and a 0.3 kJ mini-sparker on
122 the 8-25 m deep shelf. Acoustic data was received by a 32-channel digital streamer with
123 hydrophone group interval of 1.5625 m. Navigation was enabled differential GPS. A total of
124 250-line km were collected with common mid-point (CMP) spacing of 0.781 m for lines on the
125 shelf and 3.125 m for lines on the insular slope. The vertical resolution is estimated at a few
126 meters. Data processing included geometry definition, trace edits, static correction, noise
127 reduction (f-k deconvolution, f-k filtering, bandpass filtering (70-1000 Hz), CMP stack, post-
128 stack phase-shift time migration, and spiking deconvolution. Horizon and fault interpretation and
129 visualization were carried out with Kingdom Suite© software. Data penetration was typically \leq
130 0.5 s (~500 m) on the slope and ≤ 0.08 s on the shelf (Fig. 4) Deeper penetration on the shelf was
131 masked by multiples due to the shallow and sometimes hard reef bottom.

132

133 Multibeam bathymetry data, collected by the NOAA ships Nancy Foster and Thomas Jefferson
134 prior to 2019 and LIDAR data collected by NOAA on the shelf (see Appendix A3 for data
135 sources), were gridded at 8 m horizontal resolution. We added these data to an existing
136 compilation of multibeam bathymetry data in the NE Caribbean (Andrews et al., 2014).

137

138 We used Synthetic Aperture Radar interferometry (InSAR) measurements of displacements in the
139 radar line-of-sight directions and combined data from different directions to estimate two

140 components of the surface displacement. InSAR measurements from satellites in this region are
141 sensitive to the east and vertical components. The data included C-band (5.6 cm wavelength) SAR
142 from the Copernicus Sentinel-1 satellites, operated by the European Space Agency (ESA), and L-
143 band (24 cm wavelength) SAR from the Japan Aerospace Exploration Agency (JAXA) Advanced
144 Land Observation Satellite-2 (ALOS-2) satellite. Two tracks of Sentinel-1 data cover the land
145 area of the seismic activity, and another track covers the area to the east. SAR and InSAR
146 processing were done with the InSAR Scientific Computing Environment (ISCE) v2 ([Rosen et al.,](#)
147 [2012](#)) starting with the single-look complex images from ESA and JAXA. Stack processing was
148 performed with ISCE on two of the Sentinel-1 tracks descending track D098 and ascending track
149 A135, for all data from July 2019 through early August 2020. Time-series analysis was conducted
150 with MintPy ([Yunjun et al., 2019](#)) to reconstruct the line-of-sight displacements for all the dates
151 on each track and to estimate the coseismic step functions at the times of the Mw 6.4 January 7,
152 2020 earthquake and the events around July 3, 2020 and better separate the earthquake
153 deformation from atmospheric effects (Fielding et al., 2017). We processed wide-swath
154 (ScanSAR) data from ALOS-2 to form a coseismic interferogram on descending path 135 using
155 the ALOS-2 application in ISCE2 (Liang and Fielding, 2017).

156

157 We combined line-of-sight (LOS) displacement estimates from the step-function fits to the
158 Copernicus Sentinel-1 time series. The LOS (ground-to-satellite vector) for the Sentinel-1
159 ascending track A135 is up and slightly north of due west, while the LOS for the descending
160 track D098 is up and slightly north of due east. We used the same reference point at 18.0°N and
161 67.0°W for both tracks. The displacements are set to zero at the reference point, and all the other
162 displacements are relative to this point. We can combine the two InSAR LOS measurements to

163 estimate two components of the surface displacements that are close to east and vertical but
164 contain a small percentage of any north displacement (Wright et al., 2004). The resulting
165 estimates for the vertical and east components of coseismic displacements were contoured for
166 easier comparison to other data. The estimated vertical component of coseismic displacements
167 due to the Mw6.4 January 7, 2020 (time-series step-function fit at that date) are shown as red
168 contours on [Fig. 5](#). The horizontal component is smaller than the vertical and not shown.

169
170 We did a similar step-function fit to the two Sentinel-1 time series for July 3, 2020. As with the
171 January step-function fit, the 12-day intervals between acquisitions on the two Sentinel-1 tracks
172 means that all deformation in the time between acquisitions cannot be separated. For the A135
173 track, the interval that contains July 3 was 07/02–07/14 and for the D098 track the interval was
174 06/30–07/12. The conversion to vertical and east components assumes that the surface
175 displacements are the same in the two step-function fits, which should be accurate if nearly all the
176 displacement was between 07/02 and 07/12. This interval includes several earthquakes, the largest
177 were a pair of Mw5.1 and 5.3 on 07/03. The estimated vertical and east components are shown on
178 [Fig. 6a](#) and [Fig. 6b](#), respectively. An area of coastal subsidence that is much smaller than the Mw
179 6.4 signal was detected near Playa Santa that may be due to the pair of Mw 5.1 and 5.3 07/03
180 earthquake offshore ([Fig. 6a](#)). The subsidence was accompanied by westward horizontal
181 component west of Playa Santa and an eastward component east of Playa Santa ([Fig. 6b](#)).

182
183 GPS time series relative to the Caribbean reference frame for 9 stations surrounding the study
184 area ([Fig. 1](#)) were downloaded from the Nevada Geodetic Laboratory ([Blewitt et al., 2018](#)). We
185 used the data that was processed with the final GPS orbits. The time series were used to evaluate

186 relative plate motions within the region and encompassed available continuous observations for
187 at least 4 years since 2008 and prior to the start of the seismic sequence.

188

189 Locations and focal plane solutions of $M_w \geq 4.5$ earthquakes in this sequence, published by the
190 Advanced National Seismic System (ANSS) Comprehensive Earthquake Catalog (ComCat)
191 (<https://earthquake.usgs.gov/earthquakes/search/> accessed February 15, 2021) have been adopted
192 for analysis here. Some alternative locations provided in the ANSS-ComCat appear to fit the
193 other data better than the preferred ones in the catalog: The alternate epicenter of the 01/06/20
194 $M_w 5.8$ earthquake, which was thought to trigger the $M_w 6.4$ earthquake is located within the
195 modeled $M_w 6.4$ fault patch from the observed InSar subsidence (dotted blue rectangle in Fig. 2),
196 discussed below, whereas the published preferred location is 5 km to the south. The alternate
197 epicenter of the $M_w 5.6$ earthquake is located within a cluster of relatively large earthquakes,
198 which followed the $M_w 6.4$ earthquake, whereas the preferred catalog epicenter is on land 14 km
199 to the north, where there were no reports of significant damage
200 (<https://earthquake.usgs.gov/earthquakes/eventpage/pr2020007010/dyfi/intensity>). The alternate
201 locations of the 12/29/2019 $M_w 4.7$, 01/03/20 $M_w 4.7$, and the 01/10/20 $M_w 5.2$ are also clustered
202 better with other earthquakes on those dates.

203

204 The epicenter of small earthquakes in Fig. 2 were relocated using the HypoDD algorithm
205 (Waldhauser & Ellsworth, 2000) using the Puerto Rico Seismic Network (PRSN) P and S
206 arrival pick data between 12/15/2019-08/19/2020. The parameters applied in the relocation
207 were as follows: maximum separation distance of 7 km, minimum observations per event 16,

208 minimum number of pairs 12. With these constraints, 7130 earthquakes were retained for
209 relocation ([Vanacore et al., 2021](#)).

210

211 **4. Observations and modeling**

212 *4.1 Seismic reflection*

213 Seismic reflection profiles crossing the insular slope show patches of surficial sediment cover
214 with a thickness of generally ≤ 0.05 s except where deposited in depressions on the flanks of
215 canyon interfluves (purple horizon in [Fig. 4](#)). The underlying sediments appear more
216 consolidated and are internally separated by unconformities, marked by green (shallower) and
217 red (deeper) unconformities. The unconformities are discontinuous within individual lines,
218 either because of poor acoustic penetration or due to collapse and tilting of small blocks, similar
219 to observations on shore ([Monroe, 1980](#); [Renken et al., 2002](#); [Mann et al., 2005](#)). The ages and
220 consistency of the unconformities within and among lines cannot be verified without borehole
221 data. Extrapolation of the lithology encountered in the top 500 m of onshore boreholes ([Renken](#)
222 [et al., 2002](#); [Trumbull and Garrison, 1973](#)), provides a general guidance to the interpretation of
223 these offshore horizons: Unconsolidated clastic sediments of Pleistocene to Holocene age overlie
224 unconsolidated to poorly-consolidated boulder to clay-size detritus of marl and limestones of
225 Pleistocene to Miocene age, which are in turn underlain by limestone deposited in a brackish to
226 shallow marine environment. This limestone may be equivalent to the Miocene-Pliocene age
227 Ponce Formation ([Monroe, 1980](#)). Late Oligocene Juana Diaz Formation of well-bedded shales
228 and sandstones may also be encountered at the base of the seismic section ([Monroe, 1980](#);
229 [Kennedy et al., 2015](#)).

230

231 The insular shelf platform is typically < 20 m deep, is rimmed by fringing reefs at the shelf edge
232 mantled by patch reefs, cays and pavement encrusted coralline algae, stony corals (*Scleractinia*)
233 and sponges ([Ballantine et al., 2008](#)). The cays and shallow shoals were often hazard to navigation
234 and interfered with data acquisition.

235

236 Faults were recognized by offsets of normally continuous sediments or lithified sedimentary
237 units and by diffractions and opaque subvertical zones of reflectivity. The faults are concentrated
238 in specific areas: Most of them are distributed 3.5-7 km seaward of the shelf edge between
239 Guayanilla and Guanica ([Fig. 2 and 4](#)). Two additional fault groups were identified, one on the
240 slope SW of Ponce Basin ([Fig. 4e](#)), and the second group at distances of 17-21 km from the shelf
241 edge ([Fig. 4c](#)). Faults were not identified elsewhere in the survey area, i.e., closer to the shelf
242 edge, and at distances of 7-17 km from the shelf edge. Apparent dips of the mapped faults range
243 from ~45° to sub-vertical. Although fault dips were observed to be variable, adjacent ones may
244 represent a single deep fault with hanging-wall antithetic deformation (e.g., [Harding, 1985](#);
245 [Withjack et al., 1995](#)).

246

247 Faults or stratigraphic disturbances, not attributable to reefs structures, were encountered on the
248 shelf, cutting surficial sediments (<0.05 s) in several clusters ([Fig. 2](#)). Two parallel seismic lines
249 offshore Punta Montalva appear to delineate two fault groups, one in the vicinity of the offshore
250 continuation of Punta Montalva Fault ([Fig. 2; Fig 4g, h](#)), and a second one farther south ([Fig. 2](#);
251 [Fig 4g, h](#)). Faults on the shelf were also encountered in within ([Fig. 4f](#)) and seaward of
252 Guayanilla Bay, as well as south of Playa Santa and La Parguera.

253

254 *4.2 Surface subsidence and displacement*

255 Subsidence due to the Mw6.4 January 7, 2020 with a maximum of 20 cm was estimated from
256 the combined InSAR time-series fits as described above (Fig. 5). The long axis of the
257 subsidence was oriented in a NE-SW- direction with amplitude increasing offshore.
258 Eyewitnesses reported permanent flooding of parts of El Faro (Fig. 5), a coastal community
259 in Guayanilla, immediately following the Mw6.4 event (C. von Hillebrandt-Andrade, NOAA,
260 , Written Comm., 2020; Pérez-Valentín et al., 2021). Permanent flooding was also documented
261 in other coastal locations in surveys conducted during the week following the earthquake
262 (green dots in Fig. 5; Allstadt et al., 2020). The vertical subsidence was modeled with
263 Coulomb 3.3 software (Toda et al., 2010) assuming an elastic half space and using the in the
264 ANSS-ComCat fault parameters (strike, dip, and seismic moment of 268° , 43° , and $5.04e18$
265 N-m, respectively) for the Mw6.4 earthquake. Modifying the rake, slip, rupture length and
266 top and bottom depths by trial-and-error significantly improved the fit to the observations.
267 The modified parameters include a rake of -72° (-58° in the event page), top and bottom
268 depths of 2 and 10 km, rupture length of 11.3 km, and a uniform slip of 1.265 m. These
269 values are close to Liu et al. (2020) estimated peak slip of 1.6 m and main slip patch between
270 3-13 km from kinematic inversion of GPS and strong motion data. We assumed a crustal
271 shear modulus of $\mu = 3e10$ Pa. Our model predicts a maximum subsidence of 0.45 cm
272 offshore centered at the upper reach of Guayanilla Canyon (Fig. 5).

273

274 Our suggested fault plane also matches the relocated micro-seismicity by Vanacore et al.,
275 (2021) from 01/07-08 (the rupture day and the following day) (Inset in Fig. 5). Micro-
276 seismicity on 01/07/20 prior to the Mw6.4 earthquake was <8.5 km depth but extended

277 downward to ~15 km after the event, suggesting that the rupture continued to propagate
278 deeper.

279

280 The U.S. Geological Survey (USGS) revised earthquake epicenter falls, however, outside the
281 surface projection of the fault plane, but an alternate epicenter determined by the PRSN,
282 listed in the ANSS-ComCat (17.9578°N, 66.8113°W, [Table A1](#)) is located near the bottom edge
283 of the modeled slip patch (Star in [Fig. 5](#) and in inset).

284

285 A second much smaller coastal subsidence (≤ 0.04 m) was detected near Playa Santa from the
286 InSAR time-series fit for 07/03/2020 ([Fig. 6](#)). This subsidence may be due to the Mw5.3 07/03
287 and/or the 07/03 Mw5.1 earthquake offshore. The subsidence was accompanied by westward
288 horizontal component west of Playa Santa and an eastward component east of Playa Santa with an
289 amplitude ≤ 8 cm. GPS station PRMI recorded a step in the horizontal displacement components
290 during the observation period with the north component being almost twice as large as the east
291 component ([Fig. 6b](#)). We had to assume however, that the horizontal motion in the InSAR
292 anomaly represents the E-W displacement component, because the satellite lines-of-sight are
293 primarily east and west. The vertical and horizontal displacements were jointly forward-modeled
294 using Coulomb 3.3 ([Toda et al., 2010](#)) by two crossing strike-slip models (rake=0°), one oriented
295 250° and dipping 50° and the other oriented 111° (parallel to the Punta Montalva fault) and
296 dipping 85°. Both modeled faults are very shallow, from 0.5 to 3.5 km and from 0.5 to 5 km and
297 have a small slip of 40 and 25 cm respectively. The fit to observations is not as good as that of
298 the Mw6.4 earthquake subsidence despite numerous trials, because (a) the focal mechanism
299 parameters of the 07/03/2020 earthquakes served as poor starting models, (b) the two datasets

300 had to be fit simultaneously, and (c) because the north displacement component is unknown. The
301 fit the subsidence and displacement amplitudes, shown in Fig. 6, required modeled seismic
302 moments that are 4 and 2 times larger than the 8.22×10^{16} N-m and 6.62×10^{16} N-m earthquakes,
303 respectively of the two 07/03/20. Note also that one of the focal mechanisms is primarily normal
304 whereas the modelled displacements have left-lateral strike slip. The discrepancy may perhaps be
305 explained by additional aseismic deformation or by observational uncertainties in the InSAR data
306 due to the small detected amplitudes.

307

308 **5. Interpretation**

309 **5.1 Progression of seismic activity**

310 Moderate-size ($\geq M_w 4.5$) earthquake activity shows a complex temporal development of both
311 strike-slip and normal faults. We grouped the activity into clusters based on adjacent earthquakes
312 within a span 24 hours of each other. Fig. 2 shows the interpreted color-coded clusters, with their
313 temporal progression following the color spectrum from purple to red (Fig. 2 inset) and the
314 modeled fault planes from InSAR data.

315

316 Earthquake activity started SE of Guayanilla on 12/28/19 and advanced to the SE with $M \leq 5$ left-
317 lateral strike-slip focal mechanisms along one or more faults. It triggered an $M_w 5.8$ strike-slip
318 earthquake on 01/06/20. These faults were located at the upper end of the 01/07/20 $M_w 6.4$ fault
319 plane derived from modeling the InSar subsidence (Fig. 5). Additional normal and strike-slip
320 ruptures that day extended the $M_w 6.4$ fault patch to the SE, perhaps along a secondary fault(s).
321 Normal and strike-slip fault ruptures, including an $M_w 5.9$ earthquake, took place along the west
322 and side of the $M_w 6.4$ patch 3-6 days later (1/10-1/13/20) and were accompanied by intense
323 micro-seismicity (not shown). Normal fault ruptures took place along the NE edge of the $M_w 6.4$

324 rupture plane on 1/20 and east of it on 05/02/20. Strike-slip rupture also initiated 10-15 km west
325 and southwest of the M6.4 patch between 01/14 and 02/04/20 (colored grey). Seismic activity
326 intensified 10-15 km west of the Mw6.4 rupture plane during June-July 2020 with some ruptures
327 probably occurring along the Punta Montalva Fault and others under the shelf. Small coastal
328 subsidence and horizontal motion, detected by InSAR and northwestward motion registered at
329 the GPS site PRMI in La Parguera, were probably caused by a pair Mw5.1 and Mw5.3
330 earthquakes on of 07/03/2020 (Fig. 6).

331
332 Several conclusions can be drawn from this sequence of events: First, the sequence is not a
333 typical foreshock-mainshock-aftershock sequence. We base this inference on two lines of
334 evidence: (a) The magnitudes of the seismic sequence did not follow Båth's Law (i.e., Båth's
335 Law states the largest aftershock is 1-1.2 magnitude levels smaller than the main shock, e.g.,
336 [Shcherbakov and Turcotte, 2004](#)). (b) The energy released during the Mw6.4 earthquake was
337 only 64% of the total energy released during the seismic sequence, assuming similar stress drop
338 during all the earthquakes.

339
340 Second, the area may be crisscrossed by intersecting network of short faults, which were
341 probably activated by the changing stress field caused by the progression of rupture along
342 different faults. Third, the earthquake sequence was probably initiated by strikes-slip fault(s) SE
343 of Guánica, and not by rupture on the Punta Montalva Fault as initially proposed ([López-](#)
344 [Venegas et al., 2020](#)), where moderate earthquakes occurred only 6 months later.

345

346 **5.2 Associating mapped faults with seismic events and fault planes**

347 The faults in the seismic reflection profiles show offsets of tens of meters, which are much larger
348 than the offset expected from the moderate earthquakes in the recent seismic activity, suggesting
349 that they represent long-term displacements. However, the nature of these displacements, such as
350 the exact fault location, dip, strike, and rake, cannot be deduced from the profiles, because
351 shallow deformation in relatively poorly consolidated sediments is often not indicative of fault
352 parameters at depth (e.g., [Harding, 1985](#); [Withjack et al., 1995](#)). Nevertheless, we can try to
353 associate the locations of observed faults with specific clusters of earthquakes and with fault
354 planes derived from the InSar data.

355

356 Faults were observed on and close to the shelf edge, but rarely on not in deeper water. Their
357 spatial distribution is similar to the spatial distribution of the 2020 seismic sequence, suggesting
358 that earthquake activity in the region is probably limited to the nearshore area. More
359 specifically, the belt of observed faults 3-7 km south of the shelf edge in the seismic data could
360 correspond to the surface projection of the fault plane responsible for the Mw6.4 normal rupture
361 (blue rectangle in [Fig. 2](#)) and/or the rupture of subsequent earthquakes within ± 24 hours. The
362 faults on the shelf south of Guayanilla Bay could have been caused by displacements along the
363 fault plane responsible for Mw6.4 earthquake (blue rectangle) or by a fault that was reactivated
364 during the 01/20/2020 earthquake cluster (green). The fault in the middle of Guayanilla Bay ([Fig.](#)
365 [4F](#)) may be the extension of one of the faults crossing the bay from west to east ([Grossman,](#)
366 [1963](#); J. Joyce, University of Puerto Rico, Written Comm., 2020). A better delineation of this
367 fault is needed because of its location under a population center and critical industrial facilities.

368

369 However, the association of other observed faults in the seismic reflection data with the locations
370 of moderate or large earthquakes is less straight forward. Several faults were observed SW of
371 Caja de Muertos Fault and Ponce Basin, but moderate-size seismic activity did not extend to that
372 area. Whether this area is still seismically active, is unknown. One possibility is that these no
373 longer active faults undergo shallow creep induced by nearby large earthquakes existing faults.
374 An example of such phenomenon (although in an active fault) is the observed shallow creep
375 deformation on the Garlock Fault, California, following the Ridgecrest earthquake 5-20 km away
376 ([Ross et al., 2019](#)).

377

378 On the other hand, observed faults on the seismic data in the western part of our study area were
379 eventually associated with moderate earthquake activity, although not at the time of our data
380 acquisition. For example, with the exception of one Mw5.2 strike-slip earthquake (grey in [Fig.](#)
381 [2](#)), seismic activity on the shelf south of Playa Santa and Punta Montalva took place three
382 months after the completion of our survey. Fault mapping is therefore a useful tool to assess the
383 locations of future seismic activity in the area.

384

385 **5.3 The role of Punta Montalva Fault in the seismic sequence**

386 The Punta Montalva Fault ([Roig-Silva et al, 2013](#)) appears to have had a little role in the
387 initiation of the 2020 seismic sequence. The seismic sequence started several km ENE of the
388 southeastern end of the fault ([Fig. 2](#)). Moderate-sized strike-slip earthquakes and micro-
389 seismicity took place along the southeastern-most 5-km of the fault during June 2020 ([Fig. 2](#)),
390 five months after the largest event. [Adames-Corraliza \(2017\)](#) studied this part of the fault in
391 detail using LIDAR and Ground Penetrating Radar and interpreted it to be active. However, the

392 rest of the 33-km-long proposed fault was not associated with either moderate or micro
393 seismicity during this seismic sequence (e.g., [Fig. 2](#)). There was also no seismic reflection
394 evidence for an extension of the fault farther to the SE beyond the shelf edge, a distance of 5-km
395 from the headland ([Fig. 2](#)). Hence, the role of the Punta Montalva fault in accommodating the
396 differential block model in SWPR is unknown. An evaluation of the potential seismic activity
397 along the entire 33-km-long strike-slip fault is important because rupture of the entire length can
398 generate an M6.9 earthquake ([Wells and Coppersmith, 1994](#)).

399

400 **6. Discussion**

401 **6.1 Longer term tectonic activity**

402 Several lines of evidence indicate that the seismic sequence in SWPR is but the latest episode of
403 a repetitive earthquake cycle, whose recurrence interval is unknown. The extension directions
404 indicated by the T-axis analysis of moderate ($M \geq 4.5$) earthquakes from the ANSS-ComCat
405 ($329^\circ \pm 10^\circ$; [Table A1](#)) are similar to those derived by [Mann et al. \(2005\)](#) from the study of
406 terrestrial fault striations in the area ([Fig. 7](#)). The extension direction of the terrestrial faults is
407 NW-to NNW, similar to the NW-SE to NNW-SSE (303° - 344°) orientation of the T-axis of all
408 the earthquakes. The age of the terrestrial faults is estimated at post-early Pliocene based on
409 cross-cutting relationships with older faults ([Mann et al., 2005](#)).

410

411 The offsets of many of the mapped faults is at least several tens of meters ([Fig. 4](#)). Given the
412 moderate magnitude of earthquakes, the observed slip on these faults cannot be the result of the
413 latest earthquakes alone. Instead, they were likely activated repeatedly accumulating their offsets
414 over many earthquake cycles.

415

416 The area of seismic activity is the only part of southern Puerto Rico where the shelf is indented
417 northward, and the shelf edge becomes as narrow as 1 km (Fig. 7). The subsidence model for the
418 Mw6.4 earthquake predicts the location of maximum subsidence to be at the headwaters of this
419 canyon (Fig. 7), and recurrent rupture of this fault could have helped create the shelf indentation
420 in this area.

421

422 The bathymetry also shows two NE-oriented bathymetric lineaments that are deeper to the NW
423 despite the general southward dip of the insular slope (dashed blue lines in Fig. 7). These
424 lineaments, and the down-to-the-NW normal displacement of many of the earthquakes' focal
425 mechanisms, including the largest Mw6.4 event, suggest relative subsidence close to shore and
426 relative uplift farther away from shore toward the SE.

427

428 The area of seismic activity is the located at the headwaters of the only large submarine canyon
429 along southern Puerto Rico, the Guayanilla Canyon. Given the lack of major terrestrial rivers
430 feeding the canyon system, the canyon system has likely developed to evacuate the sediments of
431 the collapsing shelf edge by repeated normal faulting. The canyon system itself might have
432 partially been affected by the repeated seismic activity, as is evident by the curious right-angle
433 meandering of the eastmost tributary of the canyon. These abrupt meanders may be controlled by
434 subsurface faults (dashed blue lines in Fig. 7). Since submarine morphology typically develops
435 over a long geological time, the presence of the shelf indentation, unique lineaments and
436 meanders are other indicators for a long-term history of seismic activity.

437

438 6.2 Diffuse tectonic boundary

439 The convergence rate and azimuth of the North American Plate with the Caribbean Plate are
440 relatively constant across the span of the 800 km of the Puerto Rico Trench with deviations
441 arising only from local variability in plate boundary orientation (Fig. 1). Nevertheless, seismic
442 coupling appears to vary significantly across the plate boundary. The sector from the longitude
443 of Mona Rift westward (Henceforth, Hispaniola) is associated with several large 20th century
444 earthquakes (e.g., ten Brink et al., 2011), with partitioning of the GPS motion between sub-
445 perpendicular convergence and sub-parallel strike slip, and with the accumulation of large strains
446 on the upper plate (Symithe et al., 2015). The sector east of the longitude of Mona Passage
447 (henceforth, Puerto Rico) is associated with smaller earthquakes, many of them showing oblique
448 slip sub-parallel to the convergence direction (ten Brink, 2005; ten Brink et al., 2011). GPS
449 velocities in Puerto Rico relative to the Caribbean plate are 1/5 those in Hispaniola and show
450 northwestward motion toward the trench (Fig. 1) (ten Brink and Lopez, 2012; Symithe et al.,
451 2015).

452
453 The difference in azimuth and magnitude of the GPS velocity between Puerto Rico and
454 Hispaniola suggests the presence of a boundary between the upper plate blocks of Hispaniola and
455 Puerto Rico. This boundary crosses the island arc, but its location and nature are poorly defined.
456 GPS block models provide a relative block motion estimate of 1-5 mm/y (e.g., Symithe et al.,
457 2015). Mann et al., 2002, Manaker et al., 2008, and others suggested that the boundary connects
458 Mona Rift to Yuma Basin. Detailed multibeam bathymetry and seismic reflection mapping show
459 a system of WNW-ESE normal faults with a nested fault-system oriented NW-SE, which
460 indicates NE-SW motion across the boundary (Chaytor and ten Brink, 2010). Ten Brink and

461 [Lopez \(2012\)](#) using GPS measurements between 2008-2011 noted that stations PRMI in SWPR
462 and MOPR on Mona Island (see [Fig. 1](#) for location) move in the direction of Hispaniola whereas
463 stations farther to the north and to the east move with the direction of the Puerto Rico block.
464 They also noted a seismicity belt extending from Mona Rift to the SE through southwest PR.
465 [Solares-Colon \(2019\)](#) used the F-test to verify the independent motion of SWPR recorded by
466 GPS with respect to the Puerto Rico block, and its similar direction to Mona Island and eastern
467 Hispaniola. The width of the accretionary wedge of Muertos Trough changes significantly at the
468 longitude of the SW corner of PR ([Granja-Bruña et al., 2009](#)). The change in the width of the
469 accretionary prism may correspond to the location of the block boundary, assuming that the
470 Muertos accretionary prism is a back-arc wedge of the Puerto Rico-Hispaniola subduction zone
471 ([ten Brink et al., 2009](#)).

472
473 We propose that the Western Puerto Rico Deformation Boundary ([Fig. 1](#)) is driven by variations
474 in seismic coupling on the Puerto Rico subduction interface, with high coupling north of
475 Hispaniola and Mona passage and almost no coupling north of Puerto Rico ([Symithe et al.,](#)
476 [2015](#)). The deformation boundary may have several deformation domains: Mona rift in the north
477 is a classical rift graben bounded by a fault on its east side and perhaps another one on its west
478 side. Mona Passage farther south exhibits NW-SE series of faults, many of them not organized in
479 a uniform fashion ([Chaytor and ten Brink, 2010](#)). Some of these faults may extend eastward on
480 land ([Grindlay et al., 2005](#)). SWPR is characterized by subdued topography and east-west valleys
481 (e.g., Lajas Valley) and faults ([Prentice, 2005](#)). The recent seismic activity, reported here,
482 describes a NW-SE extension offshore SWPR. It may connect to the Muertos back-arc
483 accretionary wedge, which is significantly wider west of the deformation boundary.

484

485 We suggest that the Western Puerto Rico Deformation Boundary is similar to a diffuse zone of
486 deformation observed in the Middle America arc (Marshall et al., 2000), where smooth
487 subducting seafloor offshore Nicaragua and northern Costa Rica changes to a rough seafloor in
488 southern Costa Rica and Panama (Fig. 8). The change affects the rate of convergence and the
489 development of a back-arc accretionary wedge north of Panama, known as the Northern Panama
490 Deformation Belt (NPDB), which overthrusts the Caribbean plate. The Central Costa Rica
491 Deformation Boundary (Marshall et al., 2000) exhibits several faulting domains with different
492 faulting styles, recurring cycles of small and moderate earthquakes, and a change in the
493 magnitude and orientation of the GPS velocity vectors from the Caribbean plate across the zone
494 of diffuse deformation and to the Panama Block. Some of the seismic cycles there have been
495 triggered by large subduction or back-arc earthquakes.

496

497 Similar elements are found in Puerto Rico. The smooth sea floor is analogous to the low-
498 coupling trench north of Puerto Rico whereas the rough seafloor is analogous to the trench west
499 of Mona Rift and in Hispaniola. Differential coupling across the subduction zone creates an
500 irregular boundary across the volcanic arc, which exhibits diffuse deformation. The NPDB is a
501 bivergent thrust wedge similar to Muertos Trough (ten Brink et al., 2009).

502

503 Alternatively, the seismic sequence of SWPR may perhaps be explained in the context of a slight
504 north-south extension across the island arc, driven by strong coupling between the arc and the
505 interior Caribbean plate and a weak coupling of the arc across the subduction zone to the north
506 (Fig. 9), leading to tilting and collapse of the forearc (ten Brink, 2005). Extension in the southern

507 part of the arc is evident by the basin morphology of Virgin Island Basin and Whiting Basin SE
508 of Puerto Rico, and the possible extension across the Investigator Fault south of Puerto Rico.
509 SWPR also has a unique valley and range-like topography, indicating a relative north-south
510 extension. The continuous pre-2020 high-resolution terrestrial GPS data (Table A2) also appear
511 to indicate opposing roughly N-S motion between pairs of stations across the two blocks in
512 question. The relative motion between western Puerto Rico's GPS station pairs PRMI versus
513 PRLT, MAYZ, and PRJC and between station pairs PRGY and PRJC (Fig. 1) is 1.7 ± 0.6 mm/y
514 $N7E^\circ \pm 11^\circ$.

515

516 **6.3 Why doesn't the deformation zone mature?**

517 The recent seismic activity shows that despite being subjected to this tectonic/structural regime
518 since perhaps post Early Pliocene, deformation continues to be accommodated along many small
519 faults and has not coalesced into a mature boundary. We can offer several hypotheses to explain
520 this observation. First, the rate of deformation at this boundary is low, perhaps 1-2 mm/y (1-2 km
521 per Ma), and therefore, the coalescence of many faults into one or a couple of major faults may
522 take a lot longer. The slow deformation rate is likely due to the slow rate of convergence
523 between the North American and Caribbean plates. It is worth noting, however, that the Central
524 Costa Rica Deformation Boundary is also considered an immature block boundary despite
525 having more than an order of magnitude faster convergence rate across the Middle America
526 Trench (Marshall et al., 2000). A second and perhaps more plausible hypothesis is that the
527 inherited island arc structure and composition, such as in Puerto Rico (Fig. 3) are anisotropic
528 because the accretion process that built these arcs is fundamentally two dimensional. The
529 anisotropic composition of the arc may promote long along-arc faults, such as strike-slip faults in

530 oblique convergence regimes, and short faults with chaotic orientations at block boundaries
531 across the arc.

532

533 **7. Conclusions**

534 The Southwestern Puerto Rico (SWPR) seismic sequence ruptured multiple short normal and
535 strike-slip faults along the insular shelf and upper slope of southwest Puerto Rico. The seismic
536 activity included many moderate-size earthquakes over a span of a year and did not follow a
537 typical main shock-aftershock sequence. InSAR-detected coastal subsidence, earthquakes
538 clustered in time and space, and sub-seafloor faults, detected in high-resolution seismic reflection
539 survey, attest to the existence of multiple rupturing faults at different orientations. Despite
540 morphological and structural indicators of a long-term deformation history of similar nature, the
541 deformation does not seem to center on one or more mature fault, perhaps because of the
542 heterogenous composition and structure across the arc. The seismic sequence may be the
543 southernmost domain of a diffuse deformation boundary between the Hispaniola and Puerto Rico
544 blocks, which also includes the domains of SWPR, eastern Mona Passage, and Mona Rift. The
545 diffuse zone, which we name the Western Puerto Rico Deformation Boundary may be analogous
546 to the Central Costa Rica Deformation Boundary and may be driven by variations in subduction
547 coupling along the Puerto Rico Trench.

548

549 **Acknowledgements and Data**

550 The logistical support of the University of Puerto Rico Department of Marine Sciences in
551 carrying out a rapid response seismic reflection survey only two months after the largest
552 earthquake in the sequence is greatly appreciated. The logistical support included the use of the

553 R/V Sultana and shore support at the department's shore lab in Isla Magueyes at no cost. We
554 thank Prof. Ernesto Otero, director, and Aldo Acosta, communication specialist, and Captain
555 Orlando Espinoza and his crew for all their generous help. Christa von Hillebrandt, and Victor
556 Huérfano helped facilitate logistical issues. This work contains modified Copernicus data from
557 the Sentinel-1A and -1B satellites provided by the European Space Agency (ESA). Original
558 ALOS-2 data and products are copyright JAXA and provided under JAXA ALOS Research
559 Announcement 6 (RA6). Part of this research was performed at the Jet Propulsion Laboratory,
560 California Institute of Technology under contract with the National Aeronautics and Space
561 Administration and supported by the Earth Surface and Interior focus area. We thank Kate
562 Allstadt and Claudia Flores, USGS, for thorough and helpful reviews. Any use of trade, firm, or
563 product names is for descriptive purposes only and does not imply endorsement by the U.S.
564 Government.

565

566

567 Earthquake data can be found in ANSS-ComCat <https://earthquake.usgs.gov/earthquakes/search/>.
568 Supplemental Table A1 lists the catalog parameters of earthquakes with $M_w \geq 4.5$ including
569 alternative locations, plotted in Fig. 2. GPS data can be found at
570 <http://geodesy.unr.edu/magnet.php>. Supplemental Table A2 lists the parameters of the stations
571 appearing in Fig. 1. Processed InSAR data can be found in [https://aria-](https://aria-share.jpl.nasa.gov/20200106-Puerto_Rico_EQ/Displacements/)
572 [share.jpl.nasa.gov/20200106-Puerto_Rico_EQ/Displacements/](https://aria-share.jpl.nasa.gov/20200106-Puerto_Rico_EQ/Displacements/). Original Copernicus Sentinel-1
573 data is available at no charge from the Copernicus Sentinels Scientific Data Hub
574 (<https://scihub.copernicus.eu/>) and is mirrored at the NASA Alaska Satellite Facility archive
575 center <https://search.asf.alaska.edu/>. Original ALOS-2 data is available from JAXA

576 (<https://auig2.jaxa.jp/ips/home>). Bathymetry data can be found in [https://doi.org/10.25921/ds9v-](https://doi.org/10.25921/ds9v-ky35)
577 [ky35](https://doi.org/10.25921/ds9v-ky35) and Andrews et al. (2014). For further details see Appendix A3. The seismic reflection data
578 is being prepared for release by the USGS -Woods Hole Science Center.

579

580 **References**

- 581 Adames-Corraliza, Á. R. (2017). Geomorphic and geophysical characterization of the north
582 Boquerón Bay-Punta Montalva fault zone: A capable fault system in southwestern Puerto
583 Rico, M.Sc. thesis, 147 pp., Univ. Puerto Rico, Mayaguez.
- 584 Allstadt, K.E., Thompson, E.M., Bayouth García, D., Irizarry Brugman, E., Hernandez, J.L.,
585 Schmitt, R.G., Hughes, K.S., Fuentes, Z., Martinez, S.N., Cerovski-Darriau, C., Perkins, J.P.,
586 Grant, A.R., and Slaughter, S.L., 2020, Field observations of ground failure triggered by the
587 2020 Puerto Rico earthquake sequence: U.S. Geological Survey data release,
588 <https://doi.org/10.5066/P96QNFMB>.
- 589 Andrews, B.D., U.S. ten Brink, W.W. Danforth, J.D. Chaytor, J-L Granja-Bruna, P. Llanes
590 Estrada, and A. Carbo-Gorosobel (2014) Bathymetric terrain model of the Puerto Rico Trench
591 and Northeast Caribbean for marine geological investigations, USGS OFR 2013-1125.
- 592 Ballantine, D. L., R. S. Appeldoorn, P. Yoshioka, E. Weil, R. Armstrong, J.R. Garcia, ... and C.
593 Lilyestrom (2008). Biology and ecology of Puerto Rican coral reefs. In *Coral Reefs of the USA*,
594 pp. 375-406. Springer, Dordrecht
- 595 Blewitt, G., W. C. Hammond, and C. Kreemer (2018), Harnessing the GPS data explosion for
596 interdisciplinary science, *Eos*, **99**, <https://doi.org/10.1029/2018EO104623>
- 597 Chaytor, J.D., and U.S. ten Brink (2010). Extension in Mona Passage, Northeast Caribbean,
598 *Tectonophys.* **493** 74-92.

599 Dascher-Cousineau, K., Lay, T., & Brodsky, E. E. (2020). Two foreshock sequences post Gulia
600 and Wiemer (2019). *Seismol. Soc. Am.* **91** 2843-2850.

601 DeMets, C., Jansma, P.E., Mattioli, G.S., Dixon, T.H., Farina, F., Bilham, R., Calais, E., Mann, P.
602 (2000). GPS geodetic constraints on Caribbean-North America plate motion. *Geophys. Res. Lett.*,
603 **27** 437–440.

604 Fielding, E. J., S. S. Sangha, D. P. S. Bekaert, S. V. Samsonov, and J. C. Chang (2017). Surface
605 Deformation of North-Central Oklahoma Related to the 2016 Mw 5.8 Pawnee Earthquake
606 from SAR Interferometry Time Series, *Seism. Res. Lett.* **88** 971-982.

607 Fielding, E.J., E. Vanacore, and A. López-Venegas (2020) SAR imaging of the coseismic and
608 postseismic deformation from the 2020 southwest Puerto Rico seismic sequence, *Geo. Soc.*
609 *Am.* Annual meeting 2020, presentation 139-4.

610 Garrison, L. E. (1969) Structural geology of the Muertos insular shelf, Puerto Rico US
611 Geological Survey OFR 69-103.

612 GEBCO Compilation Group. (2020). GEBCO 2020 grid [https://doi.org/10.5285/a29c5465-](https://doi.org/10.5285/a29c5465-b138-234d-e053-6c86abc040b9)
613 [b138-234d-e053-6c86abc040b9](https://doi.org/10.5285/a29c5465-b138-234d-e053-6c86abc040b9)

614 Geist, E.L. and ten Brink, U.S., (2021) Earthquake Magnitude Distributions on Northern
615 Caribbean Faults from Combinatorial Optimization Models, *J. Geophys. Res.*, in Review.

616 Granja-Bruña, J. L., U. S. ten Brink, A. Carbó-Gorosabel, A. Muñoz-Martín, M. Gómez
617 Ballesteros (2009). Morphotectonics of central Muertos thrust belt and Muertos Trough
618 (northeastern Caribbean), *Mar. Geol.* **263** 7-33. doi:10.1016/j.margeo.2009.03.010.

619 Grindlay, N. R., L. J. Abrams, L. Del Greco, and P. Mann (2005). Toward an integrated
620 understanding of Holocene fault activity in western Puerto Rico: constraints from high-

621 resolution seismic and sidescan sonar data. Active Tectonics and Seismic Hazards of Puerto
622 Rico, the Virgin Islands, and Offshore Areas, *Geol. Soc. Am Spec. Pap.* **385**, 139-160.

623 Grossman, I. G., 1963, Geology of the Guanica-Guayanilla Bay area, southwestern Puerto Rico:
624 Art. 29 in *U.S. Geol. Survey Prof. Paper* **475-B**, p. B114-B116

625 Harding, T. P. (1985). Seismic characteristics and identification of negative flower structures,
626 positive flower structures, and positive structural inversion. *AAPG Bulletin*, **69**, 582-600.

627 Kay, C.A. (1957), Notes on the structural geology of Puerto Rico, *Bull. Geol. Soc. Am.* **68** 103-
628 118.

629 Kennedy, B.R.C., K. Cantwell, D. Sowers, A.M. Quattrini, M. J. Cheadle, and L. McKenna
630 (2015). EX1502 Leg 3 Océano Profundo 2015: Exploring Puerto Rico’s Seamounts,
631 Trenches, and Troughs, Expedition Report, NOAA Office of Ocean Exploration and
632 Research, Silver Spring.

633 Liang, C., and E. J. Fielding (2017), Measuring Azimuth Deformation With L-Band ALOS-2
634 ScanSAR Interferometry, *IEEE Trans. Geosci. Remote Sensing* **55** 2725-2738,
635 doi:10.1109/TGRS.2017.2653186.

636 Liu, C., T. Lay, T., Z. Wang, and X. Xiong (2020). Rupture process of the 7 January 2020, MW
637 6.4 Puerto Rico earthquake. *Geophys. Res. Lett.* **47** e2020GL087718.

638 López-Venegas, A.M., E. Vanacore, S. K. Hughes (2020a), Puerto Rico’s Winter 2019-2020
639 Seismic Sequence Leaves the Island On Edge, *Temblor*, <http://doi.org/10.32858/temblor.064>.

640 López-Venegas, A.M., E. Vanacore, S. K. Hughes, G. Báez- Sánchez, and T. R. Hudgins
641 (2020b), Response and initial scientific findings from the southwestern Puerto Rico Seis^[1]mic
642 Sequence” (2020), *Temblor*, <http://doi.org/10.32858/temblor.068>.

643 Manaker, D. M., E. Calais, A. M. Freed, S. T. Ali, P. Przybylski, G. Mattioli, P. Jansma, C.
644 Prépetit, and J. B. De Chabaliér (2008), Interseismic Plate coupling and strain partitioning in
645 the Northeastern Caribbean, *Geophys. J. Int.* **174** 889-903 246X.2008.03819.x.

646 Mann, P., E. Calais, J.-C. Ruegg, C. DeMets, and P.E. Jansma, (2002) Oblique collision in the
647 north-eastern Caribbean from GPS measurements and geological observations. *Tectonics* **21**
648 7-1.<http://dx.doi.org/10.1029/2001TC0011304>.

649 Mann, P., J. C. Hippolyte, N. R. Grindlay, and L. J. Abrams, (2005). Neotectonics of southern
650 Puerto Rico and its offshore margin. Active tectonics and seismic hazards of Puerto Rico, the
651 Virgin Islands, and offshore areas, *Geol. Soc. Am Spec. Pap.* **385**, 173-214.

652 Marshall, J.S., D.M. Fisher, and T.W. Gardner (2000) Central Costa Rica deformed belt:
653 Kinematics of diffuse faulting across the western Panama block. *Tectonics* **19** 468-492.

654 Miranda, E. et al. (16 authors) StEER Puerto Rico M6.4 earthquake 7 January 2020 preliminary
655 virtual reconnaissance report (PVRP), NHERI DesignSafe Project ID: PRJ-2670, Released:
656 January 10, 2020

657 Monroe, W. H. (1980). Geology of the middle Tertiary formations of Puerto Rico U.S.
658 Geological Survey Prof. Pap 953.

659 Morales-Velez, A.C., J. Bernal, K.S. Hughs, M. Pando, J.C. Perez, L.A. Rodriguez, and L.E.
660 Suarez, Geotechnical Reconnaissance of the January 7, 2020 M6.4 Southwest Puerto Rico
661 Earthquake and Associated Seismic Sequence, Geotechnical Extreme Event Reconnaissance
662 Report (GEER)-066. June 26, 2020.

663 Pérez-Valentín, K., Barreto-Orta, M., Castro, A., Montañez-Acuña, A., and Cabrera-Valentín, N.
664 (2021). Revealing geomorphic changes after the occurrence of a seismic event on the south
665 coast of Puerto Rico (2020), *Shore and Beach*, **89**, 22-33.

666 Piety, L. A., J. R. Redwine, S. A. Derouin, C. S. Prentice, K. I. Kelson, R. E. Klinger, and S.
667 Mahan (2018) Holocene Surface Ruptures on the Salinas Fault and Southeastern Great
668 Southern Puerto Rico Fault Zone, South Coastal Plain of Puerto Rico, *Bulletin of the*
669 *Seismological Society of America*, **108** 619–638, doi: 10.1785/0120170182

670 Prentice, C. S., and P. Mann (2005). Paleoseismic study of the South Lajas fault: First
671 documentation of an onshore Holocene fault in Puerto Rico, *Geol. Soc. Am. Spec. Pap.* **385**
672 215–222.

673 Renken, R. A., B. A. Black, W. C. Ward, I. P. Gill, F. Gómez-Gómez, and J. Rodríguez-
674 Martínez (2002). Geology and hydrogeology of the Caribbean islands aquifer system of the
675 commonwealth of Puerto Rico and the US Virgin Islands. US Geological Survey Prof. Pap.
676 1419.

677 Roig-Silva, C. M., E. Asencio, and J. Joyce (2013). The northwest trending North Boquerón
678 Bay-Punta Montalva fault zone—A through going active fault system in southwestern Puerto
679 Rico, *Seismol. Res. Lett.* **84** 538–550.

680 Rosen, P. A., E. Gurrola, G. F. Sacco, and H. Zebker (2012), The InSAR Scientific Computing
681 Environment, paper presented at 9th European Conference on Synthetic Aperture Radar,
682 Nuremberg, Germany, 23-26 April.

683 Ross, Z. E., B. Idini, Z. Jia, O. L. Stephenson, M. Zhong, X. Wang, ... and J. Jung (2019).
684 Hierarchical interlocked orthogonal faulting in the 2019 Ridgecrest earthquake sequence.
685 *Science* **366** 346-351

686 Shcherbakov, R. and D.L. Turcotte (2004). A modified form of Bath's law. *Bull. Seismol. Soc.*
687 *Am.* **94** 1968-1975.

688 Solares-Colón, M.M., (2019), New Constraints on Crustal Deformation Within the Puerto Rico-
689 Virgin Islands Microplate Using Two Decades of GPS Data, Ms.C. thesis, University of
690 Puerto Rico, Mayaguez.

691 Symithe, S., E. Calais, J. B. de Chabalier, R. Robertson, and M. Higgins (2015), Current block
692 motions and strain accumulation on active faults in the Caribbean, *J. Geophys. Res.: Solid*
693 *Earth*, **120** 3748-3774 <https://doi.org/10.1002/2014JB011779>.

694 ten Brink, U.S. (2005). Vertical motions in the Puerto Rico trench and Puerto Rico and their
695 cause, *J. Geophys. Res.* **110**, B06404, doi:10.1020/2004JB003459.

696 ten Brink, U.S., S. Marshak, and J.-L. Granja Bruña, (2009). Bivergent thrust wedges surrounding
697 oceanic island arcs: Insight from observations and sandbox models of the northeastern
698 Caribbean plate, *Geol. Soc. Am. Bull.* **121** 1522-1536. doi:10.1130/B26512.1.

699 ten Brink, U.S., W.H. Bakun, and C.H. Flores (2011). Historical perspective on seismic hazard to
700 Hispaniola and the NE Caribbean, *J. Geophys. Res.* **116**, B12318, doi:10.1029/2011JB008497.

701 ten Brink, U.S., and Lopez-Venegas, A.M. (2012). Plate interaction in the NE Caribbean
702 subduction zone from continuous GPS observations, *Geophys., Res. Lett.* **39**, L10304,
703 doi:10.1029/2012GL051485.

704 Toda, S., Stein, R.S., Sevilgen, V., and Lin, J., 2011, Coulomb 3.3 Graphic-rich deformation and
705 stress-change software for earthquake, tectonic, and volcano research and teaching—user guide:
706 U.S. Geological Survey Open-File Report 2011–1060, 63 p.

707 Trumbull, J. V. and L.E. Garrison (1973) Geology of a system of submarine canyons south of
708 Puerto Rico. *J. Res. U.S. Geol. Sur.* **1** 293-299.

709 Vanacore, E. A., Joyce, J., ten Brink, U., Fielding, E. J., Lopez-Venegas, A. (2021) Double
710 Difference relocations of the Southwestern Puerto Rico Seismic Sequence, *Seis. Res. Lett.*, 92,
711 1444.

712 von Hillebrandt-Andrade, C. G., A. López, E. Vanacore (2020), 2019-2020 Southwestern Puerto
713 Rico Seismic Sequence, *TsuInfo Alert*, **22**, no. 1.

714 Waldhauser, F., & Ellsworth, W. L. (2000). A double-difference earthquake location algorithm:
715 Method and application to the northern Hayward fault, California. *Bulletin of the*
716 *Seismological Society of America*, 90(6), 1353-1368.

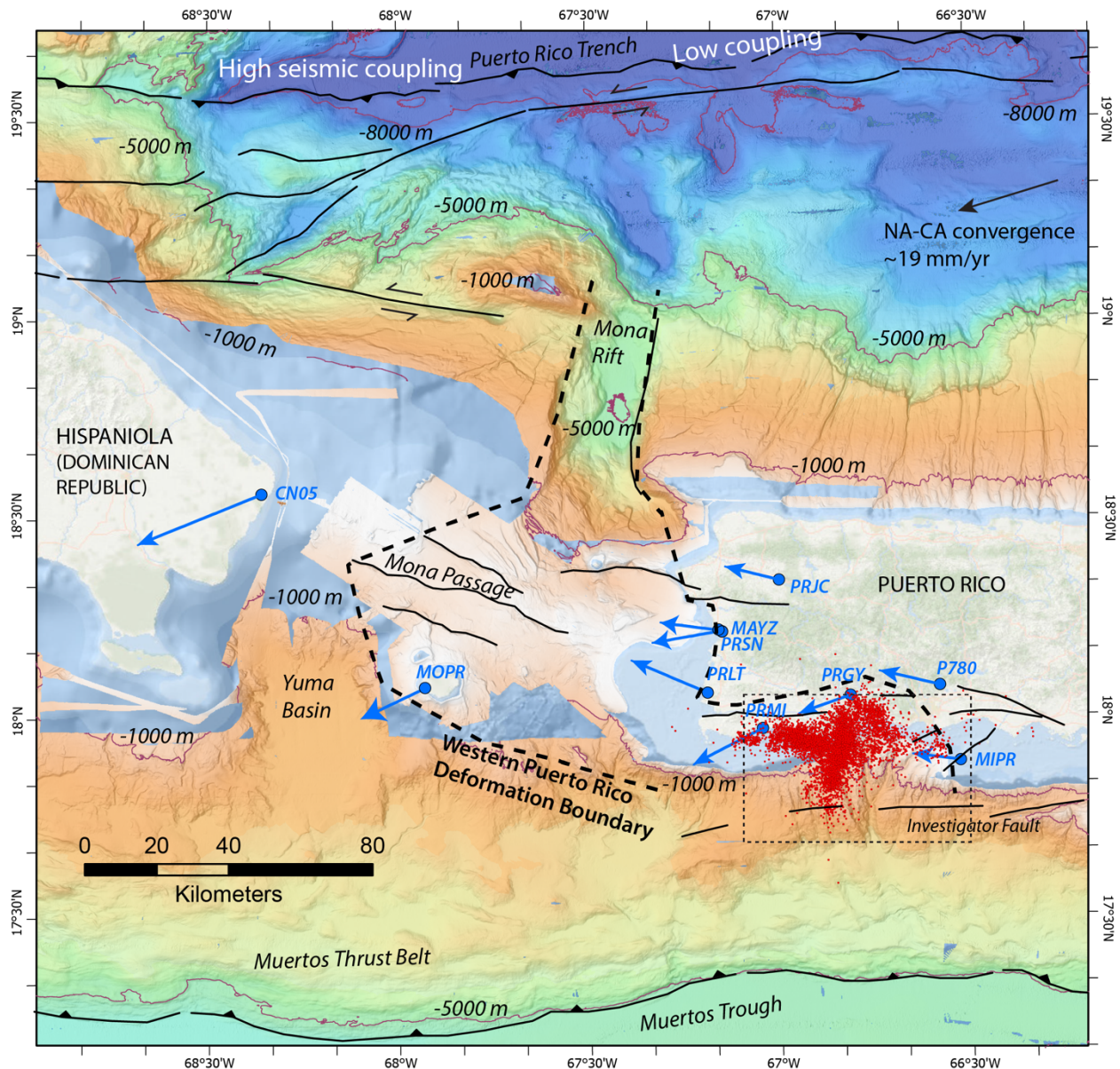
717 Wells, D.L., and K.J. Coppersmith (1994) New Empirical Relationships among Magnitude,
718 Rupture Width, Rupture Area, and Surface Displacement, *Seismol. Soc. Am.* 84 974–1002.

719 Withjack, M. O., Q. T. Islam and P.R. La Pointe (1995). Normal faults and their hanging-wall
720 deformation: an experimental study. *AAPG bull.* **79** 1-17.

721 Wright, T. J., B. E. Parsons, and Z. Lu (2004). Toward mapping surface deformation in three
722 dimensions using InSAR, *Geophysical Research Letters* **31** L01607.

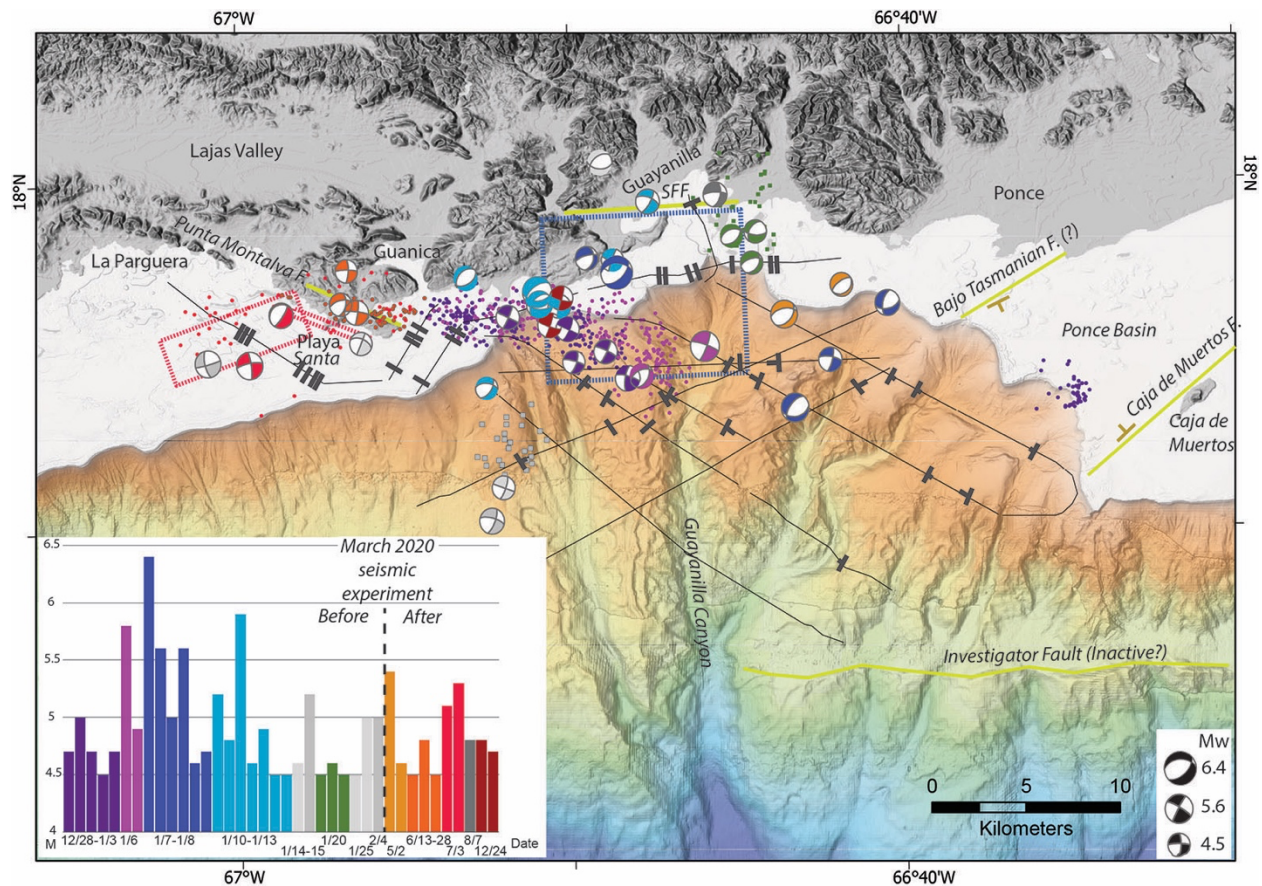
723 Yunjun, Z., H. Fattahi, and F. Amelung (2019), Small baseline InSAR time series analysis:
724 Unwrapping error correction and noise reduction, *Computers & Geosciences* **133** 104331,
725 doi:10.1016/j.cageo.2019.104331.

726



727

728 **Figure 1.** Regional map. Shaded multibeam bathymetry (Andrews et al., 2014) colored by water
 729 depth with selected depth contours (thin purple lines. Areas without multibeam bathymetry from
 730 GEBCO global bathymetry and are shaded light blue. Red dots – $M \geq 2.5$ earthquakes in the
 731 SWPR seismic sequence from ANSS-ComCat. Black lines – Major faults after Geist and ten
 732 Brink, 2021). Blue lines- GPS vectors with length proportional to long-term displacement rate
 733 relative to fixed Caribbean plate (Table A2). Area between dashed lines is our proposed Western
 734 Puerto Rico Deformation Boundary. dotted black rectangle – Location of Fig. 2.



735

736 **Figure 2.** Locations and focal mechanisms of $M_w \geq 4.5$ earthquake clusters (from ANSS-ComCat)

737 colored by date. Inset shows dates of the clusters and color code. Grey earthquakes are

738 moderate earthquakes not associated with a cluster. Some alternate epicenters from the catalog

739 are shown, as discussed in the text and listed in [Table A1](#). Colored dots – Relocated

740 microseismicity using HypoDD ([Vanacore et al, 2021](#)) for a few selected dates, with colors

741 matching the dates of focal mechanisms and the inset. Thin lines – locations of seismic reflection

742 profiles collected between 03/07-03/13/2020, Heavy black marks – Faults interpreted from the

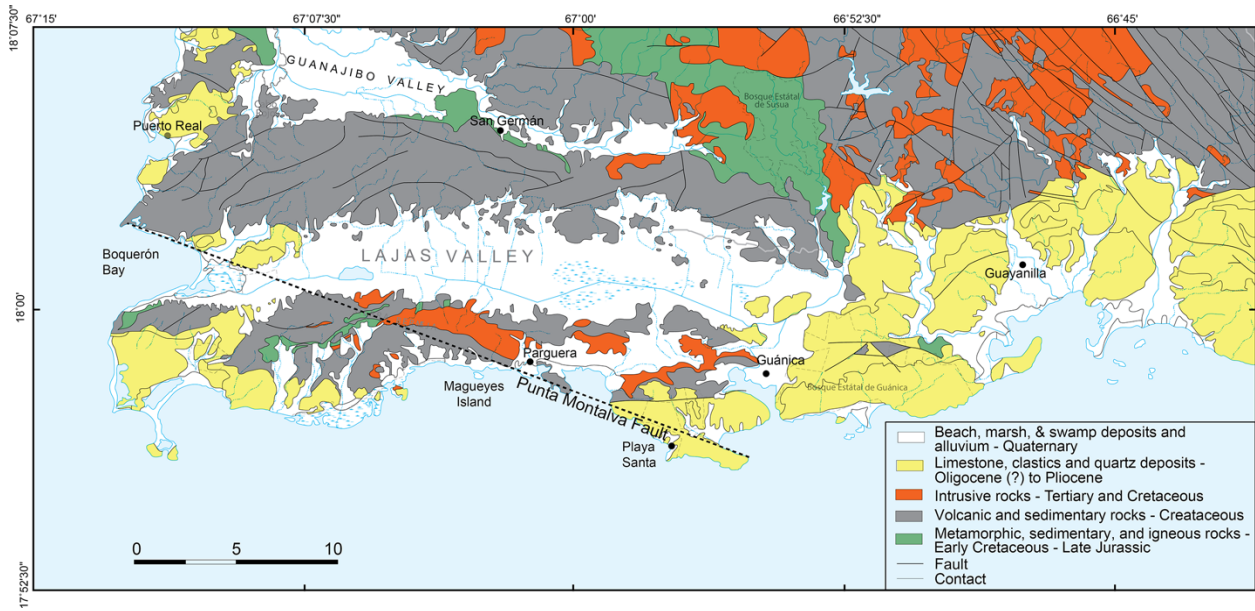
743 seismic reflection profiles with small perpendicular marks denoting apparent dip direction.

744 Dotted rectangles – Modeled fault planes from the InSAR observations ([Fig. 5 and 6](#)) with colors

745 matching the dates of the focal mechanisms and inset. Yellow lines – published faults.

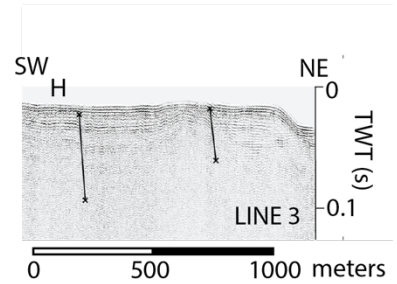
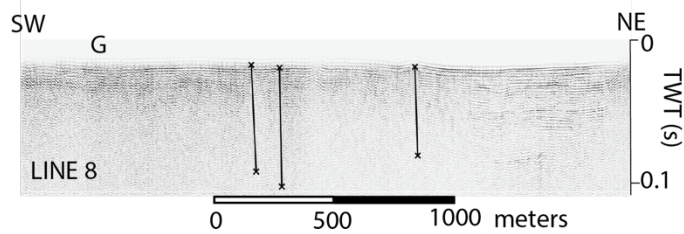
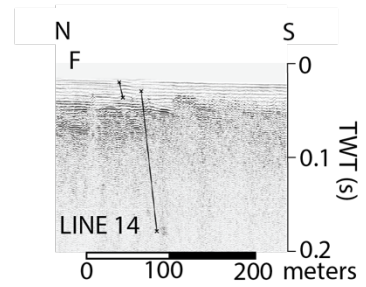
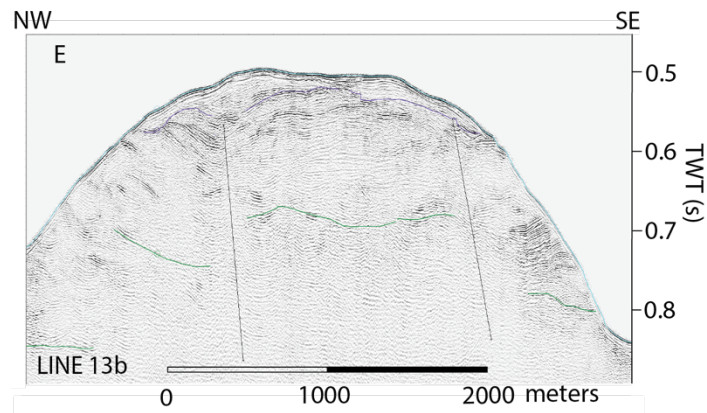
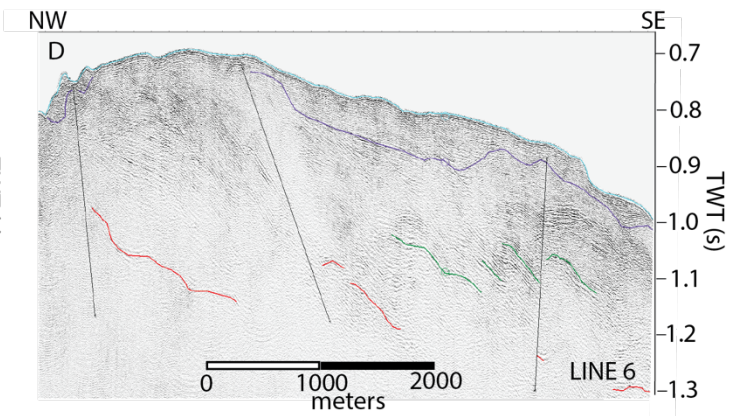
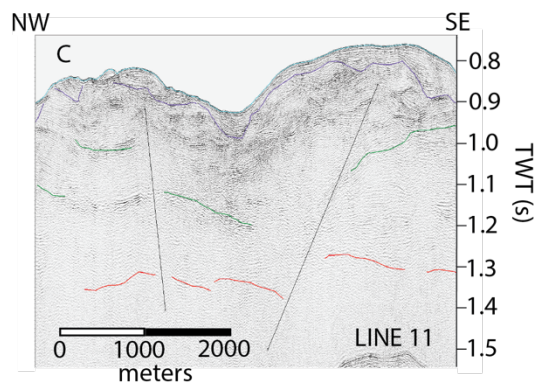
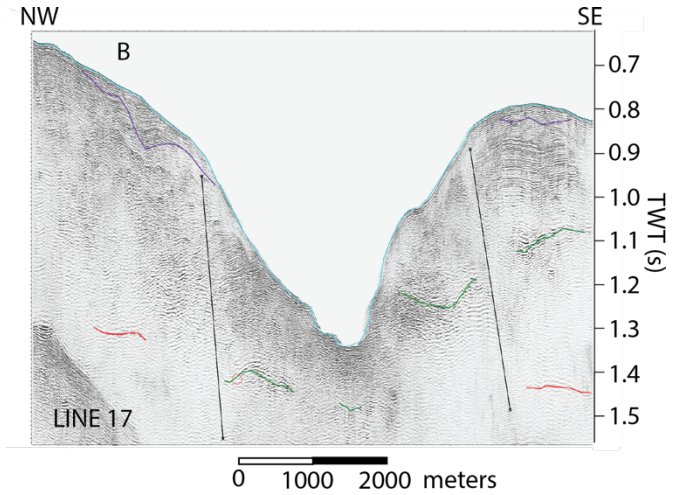
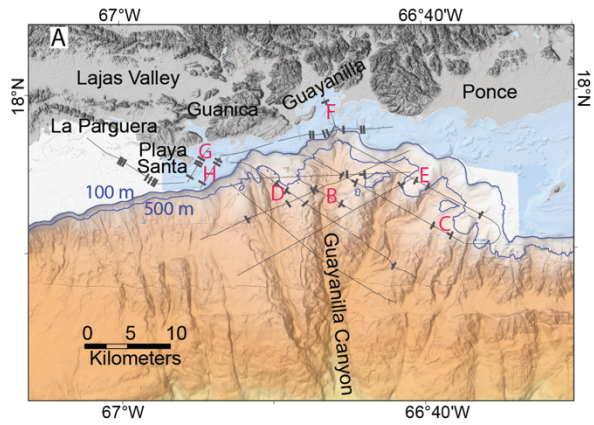
746 Background – Shaded bathymetry colored by depth (white -1 0m to blue – 2000 m) and SRTM
747 hill-shaded topography (grey). SFF – San Francisco Fault.

748



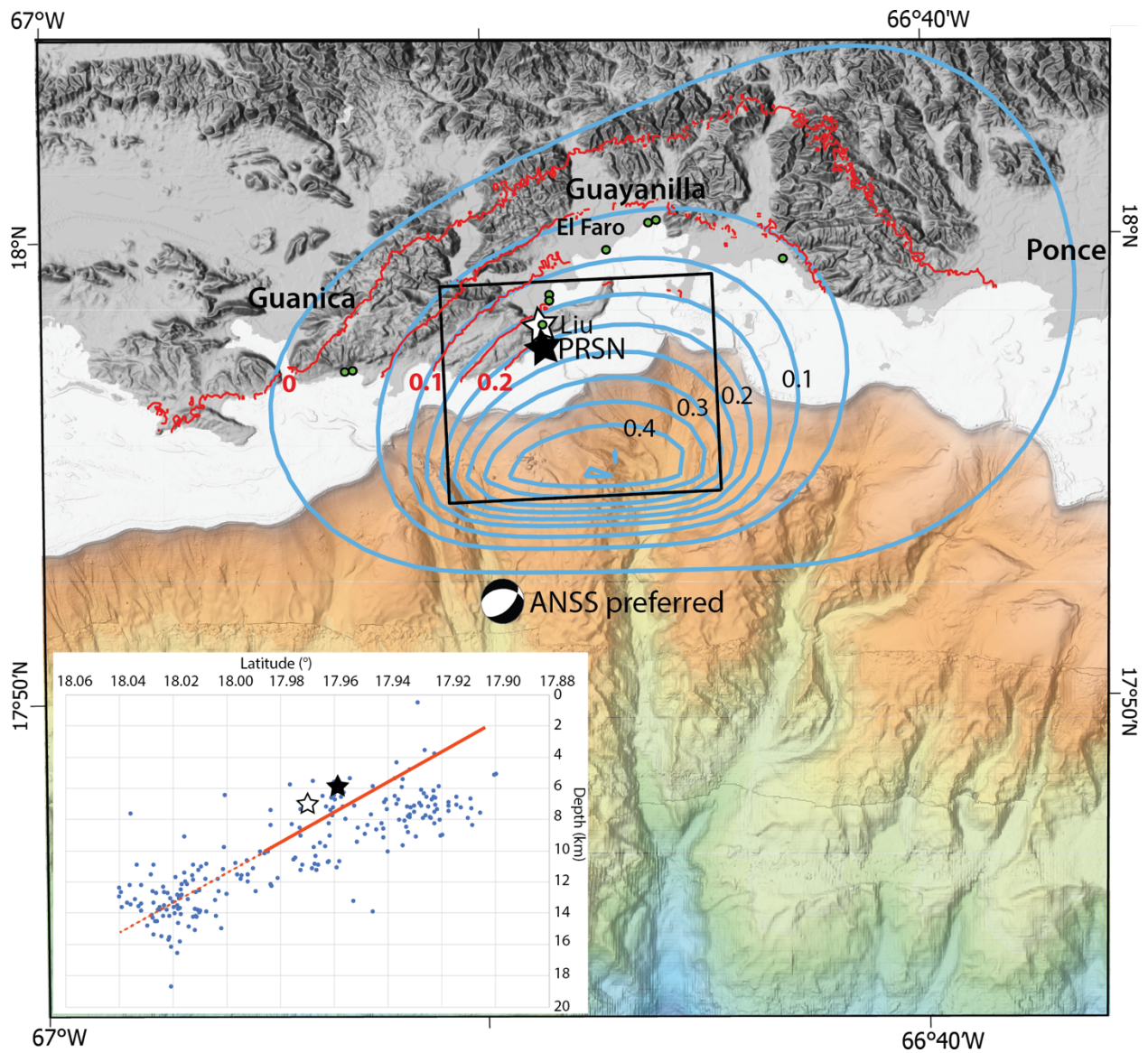
749

750 **Figure 3.** Simplified geological map of SWPR modified from *Renken et al., (2002)*. Note that
751 basement rocks (orange, grey and green) do not align along a N-S axis. Dotted line – proposed
752 33-km-long Punta Montalva Fault by *Roig-Silva et al., (2013)*.



754 **Figure 4.** *A – Location map of the seismic records. Thin lines – locations of seismic reflection*
755 *profiles. Heavy black marks – Faults identified on the seismic reflection profiles with small*
756 *perpendicular marks denoting dip direction. Blue lines – 100 and 500 m contours of water*
757 *depth, above which limited sound source output was limited. B, C, D, E - Portions of selected*
758 *high-resolution seismic profiles on the insular slope. F, G, H - Same on the shelf. Colored*
759 *horizons are interpretation of unconformities. Purple horizon separates a possible*
760 *unconsolidated Pleistocene and Holocene sediment from the underlying consolidated Late*
761 *Oligocene(?) to Pleistocene limestones and perhaps sandstone and shale. Assuming a sub-*
762 *seafloor seismic velocity of 2000 m/s, 100 milliseconds of two-way travel time (TWT)*
763 *corresponds roughly to 100 m in the sub-seafloor.*

764

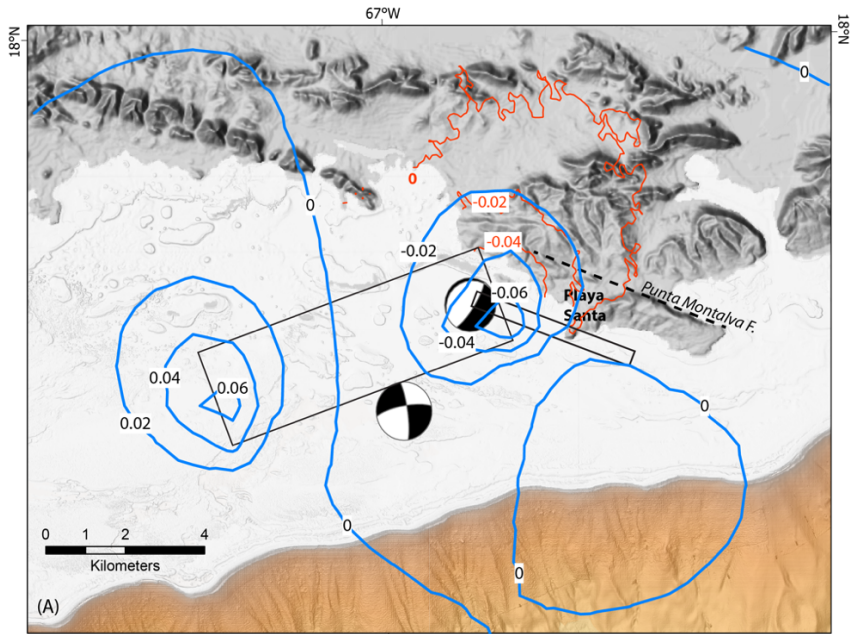


765 67°W 66°40'W

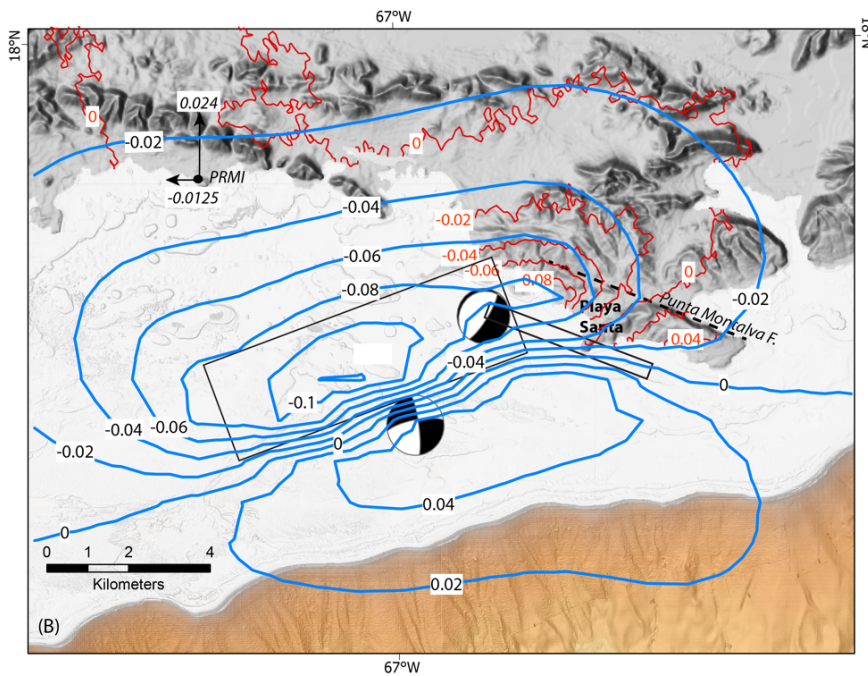
766 **Figure 5.** Comparison between InSAR subsidence observations for the period 01/02-01/14/2020
 767 (red contours) and subsidence modeling (blue contours). Contour interval for both is 0.05 m.
 768 Black rectangle -Surface projection of the modeled fault plane. The fault plane dips 43° to the
 769 north. See text for modeled fault parameters. Note that the preferred epicenter in the ANSS-
 770 ComCat is 5 km south of the updip edge of the fault plane, whereas the PRSN epicenter is
 771 located toward the bottom of the fault patch. Liu – Liu et al. (2020) epicenter (17.97°N,
 772 66.81°W). Green dots – reported locations of coastal subsidence following the earthquake. Inset

773 -Projection of relocated small earthquakes by *Vanacore et al. (2021)* occurring within the
774 longitudes of the modeled fault patch during 01/07-01/08/2020. Red line is our modeled fault
775 plane. Dashed red line is an extrapolation to deeper depths. Black and white stars - Projected
776 hypocenters of PRSN and Liu et al. respectively.

777

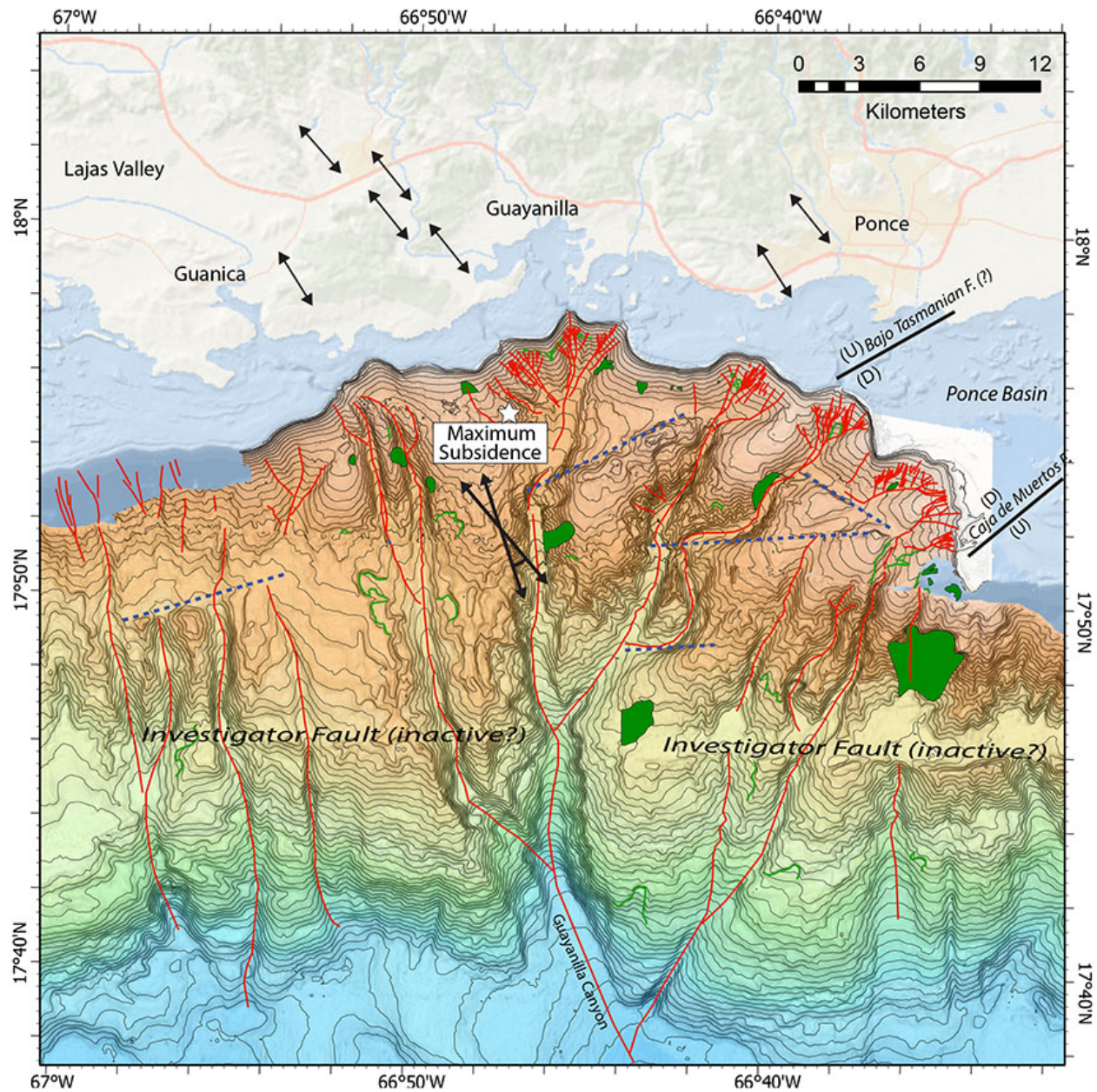


778



779

780 **Figure 6.** (A) Comparison between InSAR subsidence observations possibly related to the 07/03
781 Mw5.1 and 5.3 earthquakes (Red contours) and modeled subsidence (blue contours). Contour
782 interval for both is 0.02 m. Black rectangles - Surface projection of the modeled fault planes.
783 Fault planes dip to the NW and the NE. See text for modeled fault parameters. Focal
784 mechanisms for the two 07/03/2020 earthquakes are from ANSS-ComCat. The catalog's
785 preferred locations are outside the modeled fault planes, about 1.5 km away, and the locations
786 plotted here are Pacific Tsunami Warning Center epicenters listed in the catalog. (B) Same for
787 the east component of displacement (east is positive). Estimated horizontal displacement was
788 assumed to represent the east component of the displacement, because of the Line-of-sight
789 orientation of the satellites at this latitude. Abrupt displacement on 07/03 recorded at GPS
790 station PRMI shows that the north component is almost twice as large as the east component (B),
791 which we did not model.
792



793

794 **Figure 7.** *Compilation of evidence suggestive of long-term seismic activity in the study area.*

795 *Dark double-sided arrows – Extension directivity of a range of T-axes for $M_w > 4.5$ earthquakes*

796 *in the seismic sequence (shown offshore) (See Table A1), and terrestrial post Early-Pliocene*

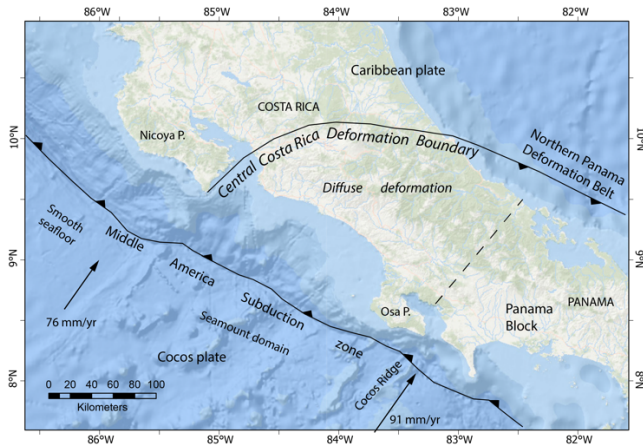
797 *faults (Mann et al., 2005). Star - Center of modeled subsidence in Fig. 5. Blue dashed lines -*

798 *Seafloor lineaments disrupting drainage on an otherwise general southward slope indicating*

799 *possible tectonic control. Red lines – Thalwegs of the drainage system. Green areas – Landslide*

800 scars. Green lines – Landslide scarps. Guayanilla Canyon is the only large submarine canyon
 801 along southern Puerto Rico, and it eroded the shelf to within 1 km from shore. Black lines –
 802 published faults and their sense of motion (after Garrison, 1969).

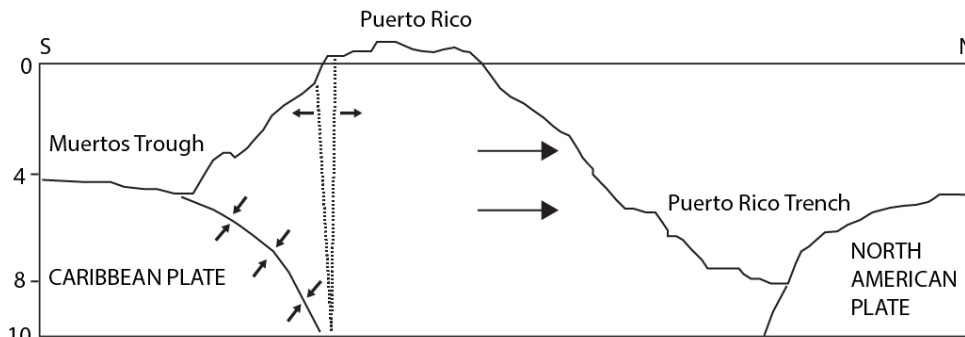
803



804

805 **Figure 8.** Simplified map of the Central Costa Rica Deformation Boundary (Marshall et al,
 806 2000), a diffuse block boundary, an analogous setting to the Western Puerto Rico Deformation
 807 Boundary.

808



809

810 **Figure 9.** An alternative explanation to the recent seismic activity in which fusion of the southern
 811 edge of the Puerto Rico block with the Caribbean plate may cause extension to develop along
 812 southwest Puerto Rico.

813

814
815
816
817
818
819
820
821
822
823
824
825
826

Supplemental material for the article

Mature diffuse tectonic block boundary revealed by the 2020 southwestern Puerto Rico seismic sequence

By U.S. ten Brink, L. Vanacore, E.J. Fielding, J.D. Chaytor, A.M. López-Venegas, W. Baldwin¹,
D. Foster, B.D. Andrews

The supplemental material includes lists of earthquake and GPS data plotted in Figures 1 and 2 and a list of bathymetry sources used to make the background bathymetry in Figures 1, 2, 4A, 5, 6, and 7.

Table A1 $M_w \geq 4.5$ from the ANSS-ComCat (<https://earthquake.usgs.gov/earthquakes/search/>) shown in Figure 2

yrmodayhrmin	Pref. lon (°W)	Pref. lat (°N)	Alt lon (°W)	Alt Lat (°N)	Moment (N-m)	Mw	Depth (km)	T axis (°)
201912282235	66.866	17.937			1.15E+16	4.7	6	340
201912290106	66.864	17.885	66.806	17.907	2.29E+16	5	6	156
201912290121	66.836	17.931			1.46E+16	4.7	3	341
202001022042	66.833	17.915			6.84E+15	4.5	7	333
202001030341	66.826	17.901	66.817	17.920	1.68E+16	4.7	2	161
202001061032	66.819	17.868	66.767	17.922	3.17E+17	5.8	6	156
200001061451	66.799	17.908			8.71E+15	4.9	6	318
202001070824	66.827	17.869	66.811	17.958	5.04E+18	6.4	9	156

202001070834	66.722	17.892			3.11E+17	5.6	10	325
202001070850	66.675	17.942			3.54E+16	5	10	313
202001071118	66.776	18.022	66.747	17.919	3.63E+17	5.6	9	164
202001071627	66.826	17.965			4.52E+15	4.6	8	320
202001082004	66.704	17.915			6.38E+15	4.7	6	147
202001102226	66.883	17.935	66.850	17.943	5.82E+16	5.2	9	161
202001110228	66.795	17.992			1.15E+16	4.8	4	158
202001111254	66.851	17.949			1.06E+18	5.9	5	339
202001112349	66.840	17.942			7.85E+15	4.6	8	325
202001120759	66.887	17.956			7.33E+15	4.9	8	143
202001121055	66.877	17.903			2.52E+15	4.5	7	335
202001130520	66.813	17.964			6.60E+15	4.5	9	335
202001141226	66.869	17.855			1.87E+16	4.6	10	336
202001151536	67.017	17.916			4.87E+16	5.2	5	123
202001200526	66.741	17.977			5.76E+15	4.5	7	157
202001200936	66.753	17.975			3.43E+15	4.6	7	149
202001201514	66.743	17.962			4.52E+15	4.5	14	327
202001250800	66.940	17.925			2.25E+15	4.5	6	152
202001252020	66.819	18.011			1.41E+16	5	13	164
202002041455	66.875	17.839			2.92E+16	5	7	153
202005021113	66.727	17.937			1.38E+17	5.4	9	332
202005021119	66.698	17.951			5.76E+15	4.6	7	325
202006130552	66.947	17.960			3.09E+15	4.5	9	317

202006280642	66.942	17.940			2.04E+16	4.8	11	322
202006282248	66.950	17.944			2.79E+15	4.5	13	315
202007031354	67.004	17.944	66.980	17.939	6.62E+16	4.9	6	129
202007032049	67.005	17.900	66.996	17.915	8.22E+16	5.3	3	126
202008070327	66.761	17.995			1.11E+16	4.8	12	325
202012241656	66.845	17.933			1.23E+16	4.8	6	334
202012241733	66.839	17.946			3.42E+15	4.7	9	328

827 Note: Pref. longitude and latitude are the preferred location provided in the catalog. Alt lon and
828 lat are alternative locations listed for these events

829

830 **Table A2.** GPS motion relative to a fixed Caribbean plate from the MAGNET GPS network

831 (<http://geodesy.unr.edu/magnet.php>) shown in Figure 1

832

Station	Long (°W)	Lat (°N)	speed (mm/y)	Azimuth (°)	East	North	SD East	SD North	Start & end dates
CN05	68.359	18.564	4.641	248	-4.310	-1.721	1.64	1.64	2014-2020
MOPR	67.931	18.077	2.508	245	-2.268	-1.071	2.16	2.05	10/08-8/11 11/14-8/16
PRMI	67.045	17.97	2.728	243	-2.432	-1.236	1.59	2.12	2016-2015
PRGY	66.814	18.051	1.907	251	-1.804	-0.618	2.57	3.24	2011-2019
MAYZ	67.159	18.218	2.042	278	-2.023	0.276	1.88	3.13	2010-2015
PRSN	67.145	18.217	2.528	261	-2.493	-0.417	2.20	2.92	2015-2019
PRLT	67.189	18.060	2.885	293	-2.604	1.126	2.05	2.41	2010-2019

PRJC	66.999	18.342	1.936	284	-1.876	0.479	2.22	2.23	2010-2019
MIPR	66.527	17.886	1.679	278	-1.663	0.228	1.52	1.68	2008-2016
P780	66.579	18.075	2.159	284	-2.099	0.509	1.94	2.17	2008-2018

833 Notes: 1. Data from 2020 was excluded from the stations in Puerto Rico, because of an observed
834 displacement step(s) in response to the seismic sequence.

835 2. SD – Standard Deviation

836

837 **Appendix A3** – Bathymetry sources used to plot Figures 1, 2, 4A, 5, 6, and 7

838

839 Cooperative Institute for Research in Environmental Sciences (CIRES) at the University of
840 Colorado, Boulder. 2014: Continuously Updated Digital Elevation Model (CUDEM) - 1/9 Arc-
841 Second Resolution Bathymetric-Topographic Tiles. [customized subset download bound by
842 coordinates 67.125 W, 18.166 N, 66.125 W, and 17.751 N]. NOAA National Centers for
843 Environmental Information, accessed March 16, 2021, at <https://doi.org/10.25921/ds9v-ky35>.

844

845 National Oceanic and Atmospheric Administration, 2006, Descriptive report, habitat and
846 hydrographic mapping survey WH00200, Puerto Rico, Northeast Caribbean Sea, vicinity of La
847 Parguera: National Oceanic and Atmospheric Administration descriptive report, variously paged,
848 accessed March 16, 2021, at <https://www.ngdc.noaa.gov/nos/W00001-W02000/W00200.html>.

849

850 National Oceanic and Atmospheric Administration, 2016, Descriptive report, navigable area
851 mapping survey H12935, Puerto Rico, Caribbean Sea, southeast coast of Puerto Rico: National

852 Oceanic and Atmospheric Administration descriptive report, variously paged, accessed March
853 16, 2021, at <https://www.ngdc.noaa.gov/nos/H12001-H14000/H12935.html>.

854

855 National Oceanic and Atmospheric Administration, 2018a, Descriptive report, habitat mapping
856 survey WH00468, Puerto Rico, Northeast Caribbean Sea, vicinity of Guanica and Ponce:

857 National Oceanic and Atmospheric Administration descriptive report, variously paged, accessed
858 March 16, 2021, at <https://www.ngdc.noaa.gov/nos/W00001-W02000/W00468.html>.

859

860 National Oceanic and Atmospheric Administration, 2018b, Descriptive report, navigable area
861 mapping survey H13143, Puerto Rico, San Juan and Ponce vicinities, Bahia de Ponce: National

862 Oceanic and Atmospheric Administration descriptive report, variously paged, accessed March
863 16, 2021, at <https://www.ngdc.noaa.gov/nos/H12001-H14000/H13143.html>.

864

865 National Oceanic and Atmospheric Administration, 2018c, Descriptive report, navigable area
866 mapping survey H13144, Puerto Rico, San Juan and Ponce vicinities, 8.5 NM SE of Bahia de

867 Ponce: National Oceanic and Atmospheric Administration descriptive report, variously paged,
868 accessed March 16, 2021, at <https://www.ngdc.noaa.gov/nos/H12001-H14000/H13144.html>.

869

870

871

872